ATLAS NOTE

June 30, 2009

Triggering on Long-Lived Neutral Particles in the ATLAS Detector

The ATLAS Collaboration

ATL-PHYS-PUB-2009-082
01 July 2009

Abstract

Neutral particles with long decay paths that decay to many-particle final states represent, from an experimental point of view, a challenge both for the trigger and for the reconstruction capabilities of the ATLAS apparatus. The Hidden Valley scenario serves as an excellent setting for the purpose of exploring the challenges to the trigger posed by long-lived particles.

1 Introduction

A number of extensions of the Standard Model result in particles that are neutral, weakly-coupled and have macroscopic decay lengths that can be comparable with LHC detector dimensions. These long-lived particles occur in many models: gauge-mediated SUSY extensions of the MSSM (addition of one singlet field), MSSM with R-parity violation, inelastic dark matter and Hidden Valley (HV) Scenarios in which a new sector is weakly coupled to the Standard Model. In the HV models long-lived HV particles that decay to heavy quark pairs and tau pairs can be produced in SUSY processes, Z' decays and Higgs boson decays [1)].

We present the results of a first study of the ATLAS Detector [1] performance for the Higgs decay $h^0 \to \pi_v^0 \pi_v^0$, where π_v^0 is neutral and has a displaced decay mainly to bottom quarks. The initial goal of our study is to obtain benchmark triggers for processes with such non-standard signatures in the ATLAS apparatus. For a description of the ATLAS trigger strategy and a description of the Level1 (L1), Level2 (L2) and Event Filter (EF) triggers see [1].

2 The Hidden Valley Scenario

Many theories of LHC-scale physics have suggested the possibility of long-lived neutral particles; for examples see [2-6]. Given that our goal is to explore the challenges to the trigger posed by such particles, the Hidden Valley (HV) scenario [7, 8, 9] serves as a useful setting: it contains many models in which such particles may appear, with a wide range of lifetimes, final states and production mechanisms.

A Hidden Valley model is structured as illustrated in Figures 1 and 2. To the Standard Model is appended a hidden sector, the "v-sector" for short [7], and a communicator (or communicators) which interacts with both sectors. A barrier (perhaps the communicator's high mass, weak couplings, or small mixing angles) weakens the interactions between the two sectors, making production even of light v-sector particles ("v-particles") rare at low energy. At the LHC, by contrast, production of v-particles, through various possible channels, may be observable.

Figure 1: A Hidden Valley model consists of a new sector neutral under the Standard Model, combined with a communicator which allows interactions between it and the Standard Model sector.

The communicator can be any neutral particle or combination of particles, including the Higgs boson, the Z boson, Z' bosons, neutralinos, neutrinos, or loops of particles charged under both Standard Model and v-sector gauge groups.

For the current study, the most important issue is the decay of the v-particles. The barrier separating

[1)] Certain models with long-lived strongly-interacting particles (R-hadrons), including split-SUSY, may produce similar signatures, if a neutral R-hadron typically decays in flight through the detector.

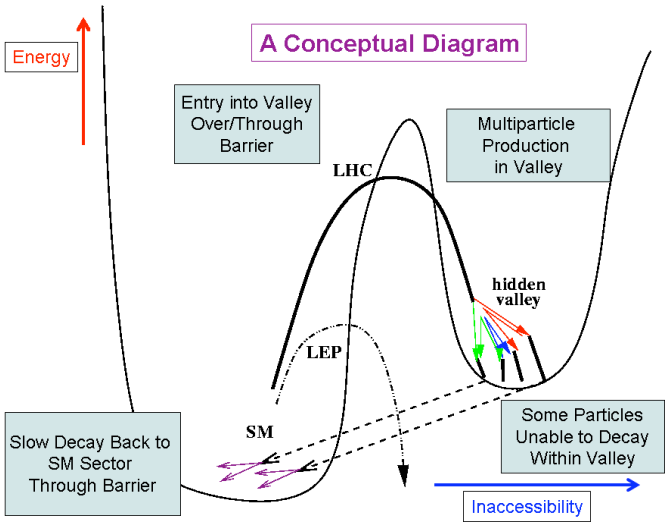

Figure 2: A hidden sector, separated from the Standard Model sector by a barrier, becomes accessible at LHC energies. The mass gap stabilizes some v-particles, allowing them to decay slowly back through the barrier to Standard Model particles.

the v-sector from our own results in long lifetimes for the lightest v-particles. These lifetimes are long relative to strong-interaction time scales, but, depending on parameters and model details, may be as short as femtoseconds or longer than microseconds. Thus, while highly displaced vertices from late decays are not guaranteed, neither are they particularly unlikely. Many HV models (though not the one we will explore below) have multiple v-particles whose lifetimes differ by orders of magnitude. Thus it is quite common that one such particle has a lifetime which puts many of its decays within the detector volume.

The study presented here is limited to the Higgs decay $h^0 \to \pi_v^0 \pi_v^0$, where π_v^0 is a neutral pseudo-scalar and has a displaced decay mainly to bottom quarks. This decay signature arises in many HV models, and moreover is not limited to the HV scenario. For instance, other non-HV models with the identical signature, where the π_v^0 is replaced with another weakly-interacting scalar or pseudo-scalar particle, were noted in [8, 10]. A third with a very similar signature – an R-parity violating supersymmetric model where the role of the π_v^0 is played by a neutralino decaying to three quarks – was noted in [11].

For our studies we use the following parameters to simulate the Higgs decay:
$E_{cm} = 10$ TeV, $m_{h^0} = 140$ GeV[2)], $m_{\pi_v^0} = 40$ GeV and $c\tau_{\pi_v} = 1.5$ m. With these parameters approximately 40% of the decays occur in the ATLAS Inner Detector (ID), 48% in the Electromagnetic and Hadronic Calorimeters and the remaining 12% in the Muon Spectrometer (MS) system.

The Higgs decay to long-lived particles is easily simulated using `PYTHIA` [12] [3)] and can be done in a number of ways. For convenience we use particles already defined within `PYTHIA`. To simulate a π_v^0

[2)] At this mass value Higgs production is dominated by gluon fusion (gg). Therefore in our simulation we have used this production mechanism. It is worthwhile to mention that this decay, if it exists, may represent an early discovery channel due to the negligible Standard Model background.

[3)] In order to properly simulate the time-of-flight of long-lived states, we changed the `PYTHIA` parameter `PARJ(71)` to allow decays throughout the entire detector volume.

particle that decays mainly to heavy flavor we make use of the A^0, that is defined in PYTHIA, as a surrogate for π_v^0. Similarly, it is convenient, instead of producing the h^0, to use the completely analogous production processes for the H^0 in PYTHIA. This avoids the various problems with PYTHIA routines especially designed for the decays of the Standard Model h^0. The H^0 mass is set to m_H, the A^0 mass to $m_{\pi_v^0}$ and the lifetime of the A^0 to the desired π_v^0 lifetime τ_{π_v}. We turn off all decays of the H^0 except $H^0 \to A^0A^0$, and allow the A^0 to decay as it normally does, to heavy flavor quarks and leptons, mainly $b\bar{b}$.

We have initiated studies (not discussed in this note) of the Z' decay into a Hidden Valley sector. The essential difference from the Higgs case just considered is that the mass scale of the Z' is much higher than that of the Higgs. Thus while the Higgs boson can produce just two v-hadrons in this study, the more massive Z' can produce many at once, with strong variability in multiplicity and kinematics.

3 Detector Signatures

The Hidden Valley particles, as discussed in [7], can have a range of lifetimes leading to the possibility of displaced $b\bar{b}$ vertices occurring throughout the entire detector volume. Figure 3 gives the probability that a π_v^0 decays in the three detector regions: Inner Detector (ID), Calorimeters and Muon Spectrometer as a function of its proper lifetime $c\tau$ for the combined barrel and forward detectors ($|\eta| \leq 2.5$), and the fraction of π_v^0's that have β_{π_v} less than the abscissa value. The distributions are from PYTHIA generated gluon fusion Higgs decays, consequently they include production and decay kinematics.

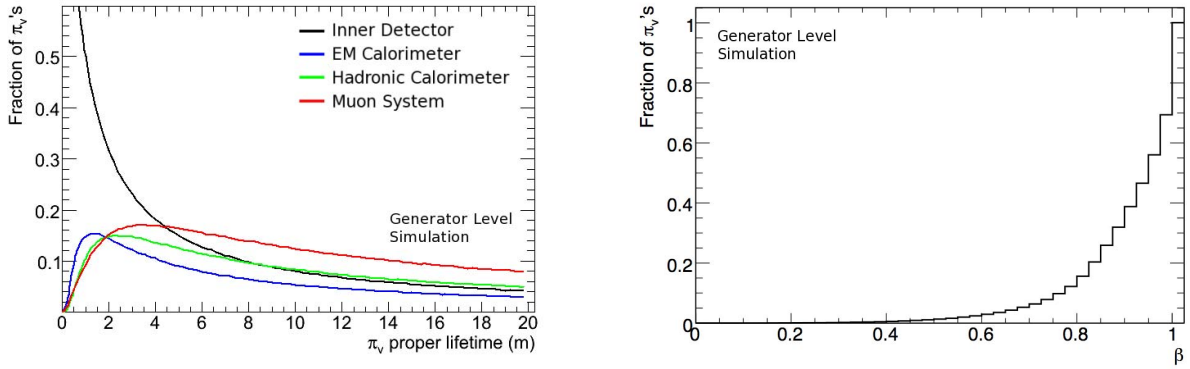

Figure 3: (Left): π_v^0 decay probability in Inner Detector, Calorimeters and Muon Spectrometer for $|\eta| \leq 2.5$; (Right): fraction of π_v^0's that have β_{π_v} less than the abscissa value.

In this section we discuss the b-jet signatures that are observed in different parts of the ATLAS detector from decays of π_v^0's to $b\bar{b}$ pairs. We consider four detector regions:

- Decays from end of the Hadron Calorimeter (HCal) to the first Muon Spectrometer trigger plane;
- Decays in the calorimeters;
- Decays in the Inner Detector beyond the pixel layers to the end of the Transition Radiation Tracker (TRT);
- Decays in the beam pipe and pixel layers.

We consider each of these regions and illustrate the trigger signatures of Hidden Valley particles using our gluon fusion produced Higgs sample. The decay of Z' bosons and neutralinos to π_v^0's will result in signatures that are topologically similar.

3.1 Decays in the Muon Spectrometer

Decays occurring near the end of the HCal and before the first muon trigger plane result in a large number of charged hadrons traversing a narrow (η, ϕ) region of the Muon Spectrometer. The L1 muon trigger will return several Regions of Interest (RoI) clustered in a small (η, ϕ) area. Figure 4 (transverse view) shows the cluster of tracks (A) observed when a π_v^0 decays before reaching the first muon trigger plane. The black points in the muon spectrometer are trigger chamber hits and the lines are track segments found by the muon track reconstruction software. Figure 5 shows a longitudinal view of a different π_v^0 decay that again clearly shows the RoI's clustered in a small (η, ϕ) region. The muon RoIs from this type of decay topology usually will not have any associated tracks in the inner tracker and most will not survive the L2 muon trigger. However, this RoI cluster event signature can be used as a stand-alone L2 trigger object to select these late decays (see section 5 for details).

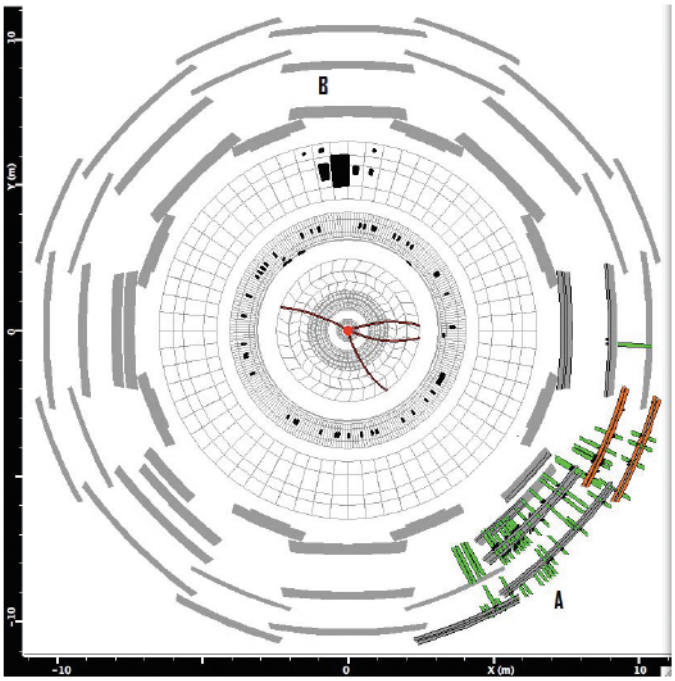

Figure 4: ATLANTIS[5)]Display (transverse view) of reconstructed event properties for two π_v^0 decays: A in the barrel muon spectrometer and B in the hadronic calorimeter.

3.2 Decays in Calorimeters

If the decays in or beyond the Electromagnetic Calorimeter (ECal) the ratio of energy deposited in the HCal to that in the ECal will be larger than that which is normally observed for jets originating at the Interaction Point (IP). This suggests $\log_{10}(E_{HAD}/E_{EM})$ as a trigger object. Figure 4 (B) illustrates this and makes very clear that for this type of event the ECal records little or no energy, while the HCal has a large energy deposition. No visible track connects this jet with the IP. An additional characteristic of this decay is the cone size of the resulting jet. As can be seen in Figure 6 almost all the energy for events decaying in the barrel HCal are contained in a $\Delta R(\eta, \phi)$[6)] cone of 0.1 around the jet axis. This suggests that an L1 tau trigger that utilizes a narrow cone can be used to select these decays.

[5)] ATLANTIS is the official ATLAS event display.

[6)] $\Delta R(\eta, \phi) = \sqrt{\Delta\eta^2 + \Delta\phi^2}$

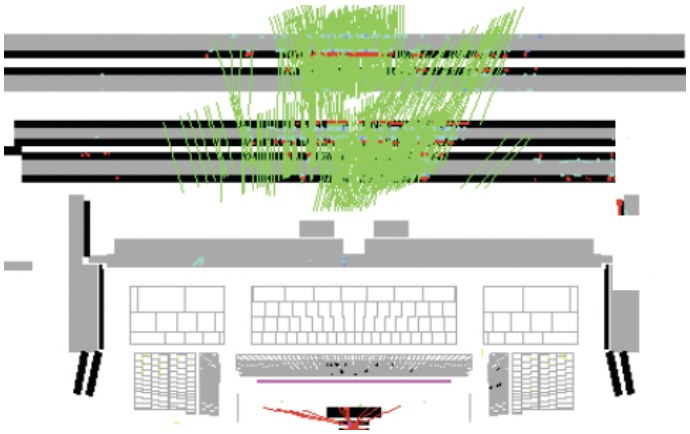

Figure 5: ATLANTIS display (longitudinal view) of a π_v^0 decay in the barrel muon spectrometer.

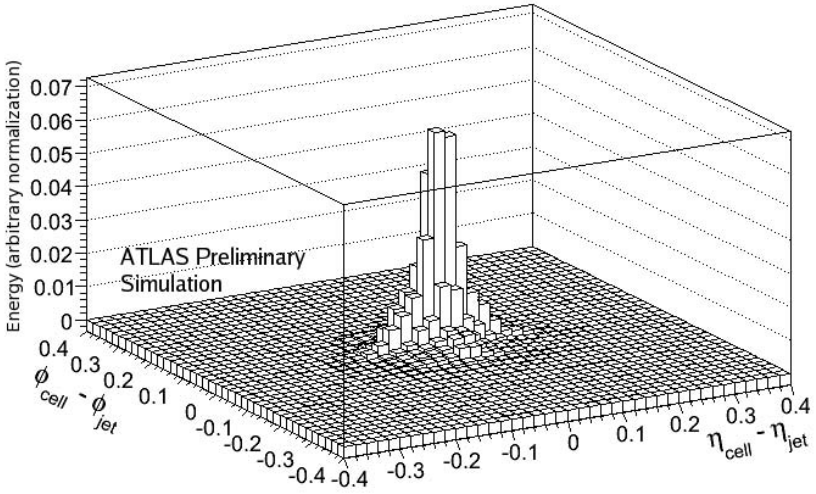

Figure 6: Lego plot of the energy deposition in the calorimeter cells around the jet axis (0,0) for π_v^0's decaying in the HCal.

3.3 Decays in TRT

Decays in the outer Silicon layers and TRT lead to jets with no connecting track to the IP (trackless jets). An example of this type of event can be seen in Figure 7, which shows the ATLANTIS display for two π_v^0's decaying in the TRT[7]. Selecting such events at L2 requires a L2 ID vertex finding algorithm using tracks with large impact parameters that is not currently available. Thus for this note we examine trackless jets as trigger objects for this event signature.

3.4 Decays in the Beam Pipe and Pixels

Decays in the Beam Pipe or in the Pixel layers will look very much like decays of heavy flavors produced in Standard Model processes. The *b*-tagging algorithms will be helpful in identifying some of these decays, but because of the low p_T of the jets the efficiency may be low. For those events that are identified

[7] Only Trigger Space Points (Silicon hits inside the RoIs) are shown.

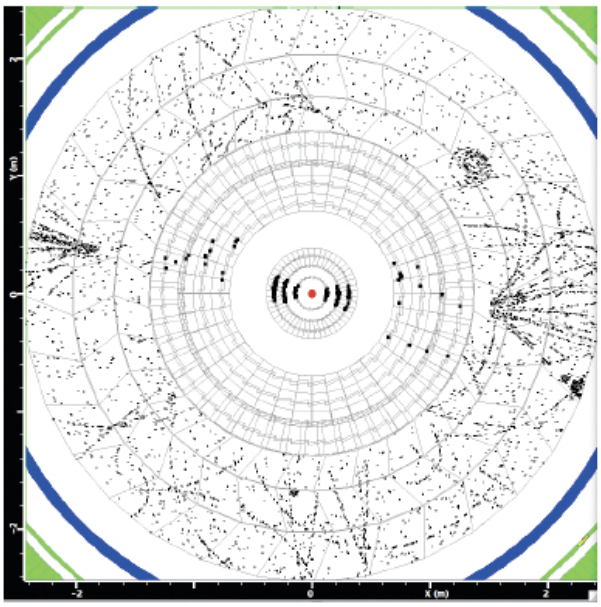

Figure 7: ATLANTIS display of the reconstructed event properties for two π_v^0 decays in the TRT, where only Silicon hits inside the RoI are shown.

by the b-tagging algorithms the challenge will be to find techniques at the Event Filter level and off-line to select these late decays from the large, potentially irreducible heavy flavor decay background. We will not discuss these events further in this paper.

4 Efficiency of Current ATLAS triggers

In order to study the efficiency of the current ATLAS triggers on events with highly displaced vertices we use two signal samples: a sample containing only signal at 10 TeV and one sample that contains signal plus pileup and cavern background for a luminosity of 10^{32} cm^{-2}s^{-1}. These are summarized in Table 1.

Dataset	N_{events}	Bunch Spacing	$< N_{pileup}$/collision$>$
No Pileup	45K	Not Relevant	0
Pileup	15K	450 ns	4.1

Table 1: HV datasets at 10 TeV c.m. energy.

For the L1 triggers we have used a combination of standard triggers that are expected to have no prescaling at least up to a luminosity of 10^{32} cm^{-2}s^{-1}. All events were simulated using ATHENA-GEANT4.

4.1 Current ATLAS Muon Triggers

The standard ATLAS L2 muon trigger consists of two algorithms, muFast and muComb[13], that are applied sequentially. Both must be passed to fire the L2 trigger. These algorithms are designed to select muons produced at the interaction region and contribute to rejecting RoIs produced from highly displaced vertices. The muFast algorithm creates track segments using the full granularity of the muon system and performs a refined p_T measurement, which reduces the number of RoIs by $\sim$30%. The effects of the muFast algorithm can be seen in Figure 8, which shows the fraction of "muon" candidates selected by

the L1 trigger and those remaining after applying the muFast algorithm.

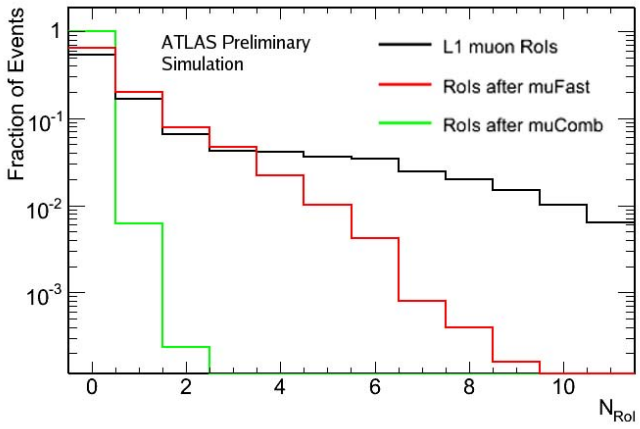

Figure 8: Fraction of muon RoIs found at L1 and after applying muFast and muComb.

The second algorithm, muComb, requires that each muon candidate found by muFast have a matching Inner Detector track. This algorithm only passes $\sim 0.5\%$ of muon candidates coming from π_v^0 decays as can be seen in Figure 8 and Table 2[8)]. This low efficiency is due to the muon candidate being produced beyond the pixel layers (perhaps even beyond the TRT), thus leaving few, if any, hits in the Inner Detector. It is clear from these rates that a dedicated signature-driven L2 muon trigger is required to keep events that are characterized by highly displaced vertices.

	L1_MU4	L1_2MU4	L1_3MU6	L2_mu4	L2_2mu4	L2_3mu6
No Pileup	45.2±0.3%	28.8±0.3%	12.9±0.2%	0.75±0.04%	0.13±0.02%	0.002±0.002%
Pileup	46.9±0.4%	29.4±0.3%	12.9±0.2%	0.88±0.05%	0.18±0.02%	0.006±0.004%

Table 2: Efficiencies of standard ATLAS L1 and L2 muon triggers. The L1_MU4 trigger is foreseen to be prescaled at the High Level Trigger (HLT), but is shown here to demonstrate the effects of the current HLT algorithms.

4.2 Current ATLAS Jet Triggers

Events in which the Higgs decays to π_v^0's are characterized by several low p_T jets. The low jet energy results in large rejection factors and a corresponding low signal efficiency for the standard non prescaled jet triggers. L1 and L2 jet triggers that are not planned to be prescaled for an instantaneous luminosity of 10^{31} cm^{-2}s^{-1} result in a total passing rate of less than 2%. From this, it is clear that we will need new signature-driven trigger algorithms in order to accept events with highly displaced jet vertices, especially at higher luminosity, where the jet trigger thresholds will be increased.

[8)] In the ATLAS convention the trigger name contains the trigger level (e.g. L1), the trigger object (e.g. MU), the number of objects (e.g. 2MU) and the corresponding energy or momentum threshold; thus L1_3MU6 is a L1 trigger requiring three muons with greater than 6 GeV transverse momentum.

5 New Trigger Objects

In the following subsections we describe three L2 signature driven triggers for decays in the Muon Spectrometer, Calorimeters and Inner Detector, respectively.

5.1 Decays in the Muon Spectrometer

Events with π_v^0's that decay near the end of the HCal or in the Muon Spectrometer are characterized by a large number of hits in the muon system with little to no energy deposited in the calorimeters. Such an event has a cluster of L1 muon RoIs centered around the decay position of the π_v^0. This is illustrated by Figure 9 that gives the average number of L1 muon RoIs in a cone of $\Delta R = 0.4$ around the π_v^0's line of flight as a function of the π_v^0 radial decay distance. As the π_v^0 decays close to the end of the HCal (4500 mm), the average number of muon RoIs contained in the cone increases rapidly due to the charged tracks from the π_v^0 decay. The number of RoIs remains large and approximately constant until the π_v^0 decays close to the first muon trigger plane (7000 mm), at which point the charged hadrons are not separated enough to give multiple, unique RoIs[9)]. Moreover, as shown in Figure 10, the π_v^0 decays in the region between the end of the HCal and the first trigger plane of the muon system are characterized by an anomalous number of L1 RoIs in a small ΔR cluster. This provides a characteristic signature for selecting such events.

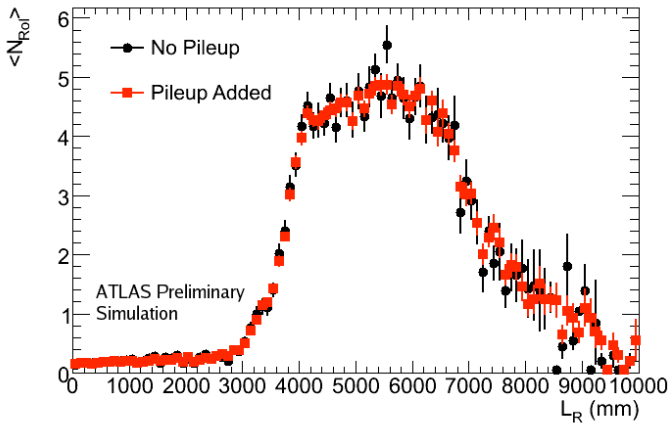

Figure 9: Average number of L1 muon RoIs vs π_v^0 decay distance.

5.2 Decays in the Calorimeters

Events with decays in the calorimeters are characterized by jets with few or no tracks in the ID and unique energy distributions. Because the jet vertex is located inside of the calorimeter, the jet decay products will be contained in a relatively small number of calorimeter cells. Figure 11 shows the energy distribution in (η, ϕ) for π_v^0's that decay inside of the barrel HCal (see also Figure 6 which gives the corresponding lego plot for these events). The narrow jets allow us to use the L1 τ trigger to lower the jet energy threshold, which increases our signal acceptance but not the amount of QCD background accepted at L1. To implement this we will make use of the L1 trigger, L1_TAU40, which selects energy clusters with $E_T > 40$ GeV that are contained in a $(\Delta\eta \times \Delta\phi)$ region of (0.2×0.2). This trigger is not

[9)] Decays beyond the first trigger plane do not give RoIs as the L1 trigger requires hits in both the first and second trigger planes; the few RoIs from decays after 7000 mm are due to low momentum curling tracks from the π_v^0 decay.

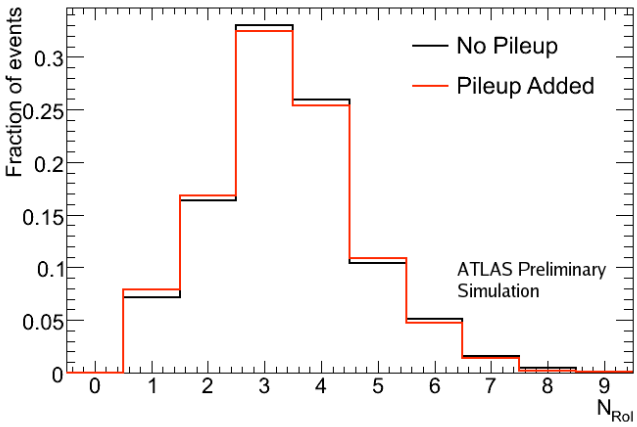

Figure 10: Number of L1 muon RoIs contained in a cone of $\Delta R = 0.4$ in events that pass the L1_3MU6 trigger.

foreseen to be prescaled up to luminosities of $10^{32}\,\mathrm{cm}^{-2}\,\mathrm{s}^{-1}$.

In addition to producing narrow jets, these events usually have little energy deposited in the first part of the ECal, which results in jets with significantly more energy deposited in the HCal than in the ECal. This is illustrated by Figure 12 that shows the distribution of the $\log_{10}$ of the Hadronic to Electromagnetic energy ratio for jets from π_v^0 decays as a function of the π_v^0 decay distance. As the π_v^0 decays closer to the end of the ECal (2200 mm), the ratio changes from a characteristic negative to a positive value and the value of $\log_{10}(E_{HAD}/E_{EM})$ plateaus at $\sim$ 1.5 until $\sim$ 3600 mm, at which point the π_v^0 decay occurs too close to the end of the Hadronic Calorimeter (4250 mm) to accurately measure the jet energy, which causes the value of $\log_{10}(E_{HAD}/E_{EM})$ to decrease.

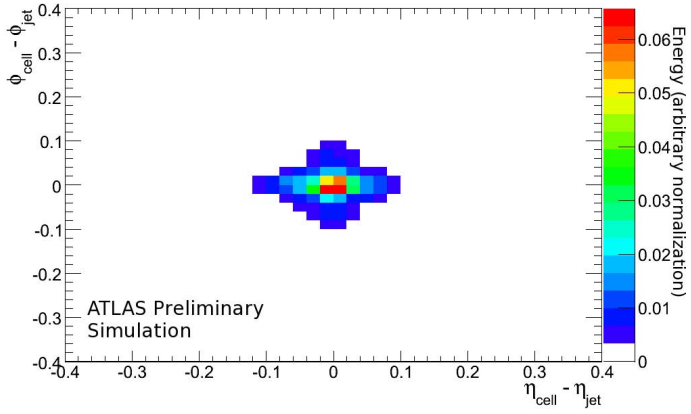

Figure 11: Energy distribution for jets that originate from π_v^0's that decay inside of the barrel HCal, where (0,0) is the jet axis.

If $\log_{10}(E_{HAD}/E_{EM})$ is plotted for each jet in the event, two distributions are clearly present (Figure 13). The distribution centered at $\sim$ -0.75 is from π_v^0 decays in the ID[10)], while the second distribution, cen-

[10)] Standard QCD jets give a similar distribution centered at $\sim$ -0.75.

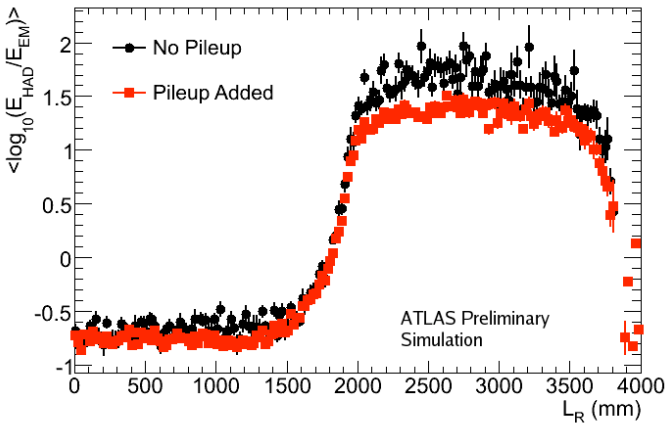

Figure 12: Mean value of $\log_{10}(E_{HAD}/E_{EM})$ for all jets coming from π_v^0 decays as a function of the π_v^0 decay position in the barrel HCal ($|\eta| < 1.4$).

tered at $\sim +1.5$, is from π_v^0 decays occurring inside of the calorimeters (see Figure 14). The separation of the two distributions suggests that $\log_{10}(E_{HAD}/E_{EM})$ could be used as a new trigger object.

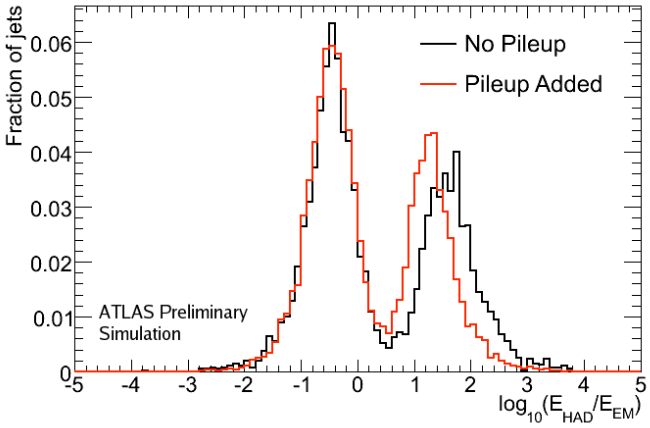

Figure 13: Distribution of $\log_{10}(E_{HAD}/E_{EM})$ for all jets in events that pass the L1_TAU40 trigger for $|\eta| < 2.5$ (pileup lowers the position of the second peak, as could be expected).

Because jets with $\log_{10}(E_{HAD}/E_{EM}) \geq 1$ are produced by π_v^0's decaying in the calorimeter, one would expect to find a lack of activity in the ID. Using the L2 tracking algorithm, SiTrack[11] [13], we find that greater than 95% of jets with $\log_{10}(E_{HAD}/E_{EM}) \geq 1$ have zero tracks with $p_T \geq 1$ GeV reconstructed in a $(\Delta\eta \times \Delta\phi)$ region of (0.2×0.2) around the center of the jet RoI, see Figure 15.

5.3 Decays in the Inner Detector

Decays of π_v^0's in the ID pose a challenge for the current tracking and vertex reconstruction algorithm used in the HLT. The current ATLAS tracking strategy [13] requires the formation of track seeds using at least three hits in the Pixel Detector and one in the first Semi-Conductor Tracker (SCT) layer, which

[11] The SiTrack algorithm reconstructs tracks with $p_T \geq 0.5$ GeV

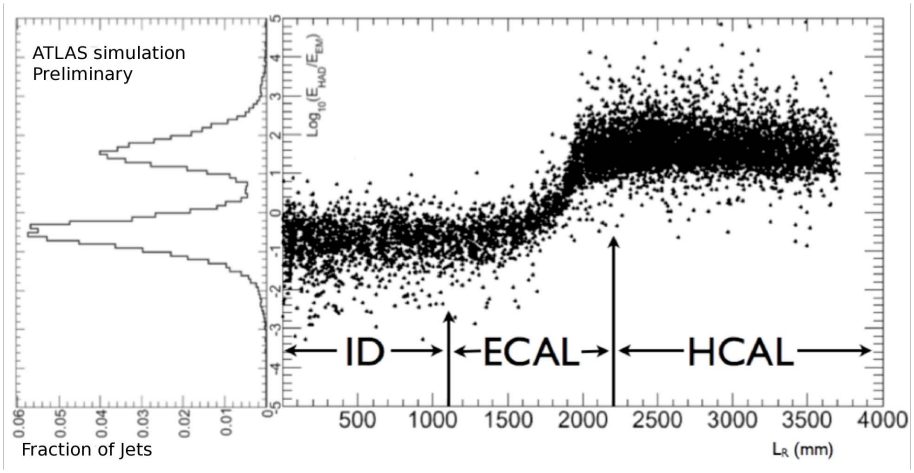

Figure 14: $\log_{10}(E_{HAD}/E_{EM})$ for all jets coming from π_v^0 decays as a function of the π_v^0 decay position in the barrel HCal ($|\eta| < 1.4$) and the projection showing the second peak from decays in the HCal.

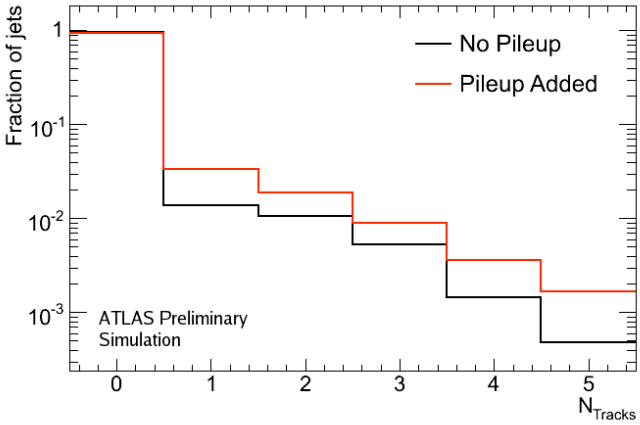

Figure 15: Number of tracks reconstructed by the L2 tracking algorithm SiTrack, using a track p_T cut of 1 GeV for events with $\log_{10}(E_{HAD}/E_{EM})\geq 1$.

significantly reduces the tracking efficiency for events where the π_v^0 decays beyond the first pixel layers. Consequently a large fraction of jets originating from π_v^0 decays have no reconstructed tracks with $p_T \geq$ 1 GeV as can be seen in Figure 16. We refer to those jets that have no reconstructed tracks with $p_T \geq 1$ GeV as 'trackless jets'. This 'trackless jet' signature is a potential trigger object. The QCD background to a 'trackless jet' trigger can be significantly reduced by requiring that the 'trackless jet' contain at least one charged particle, a muon, in the jet cone. In Standard Model jets that originate at the IP, the muon will typically be prompt and leave a track in the ID spoiling the trackless requirement, whereas in events with displaced decays, the muon will be produced beyond the innermost tracking layers and thus have no reconstructible ID track. A trackless jet with a muon in the jet cone is the trigger object. We note that muons are present in only about 15 to 20 percent of b decays. This reduces the maximum possible efficiency to about 30 to 40 percent for a π_v^0 decay.

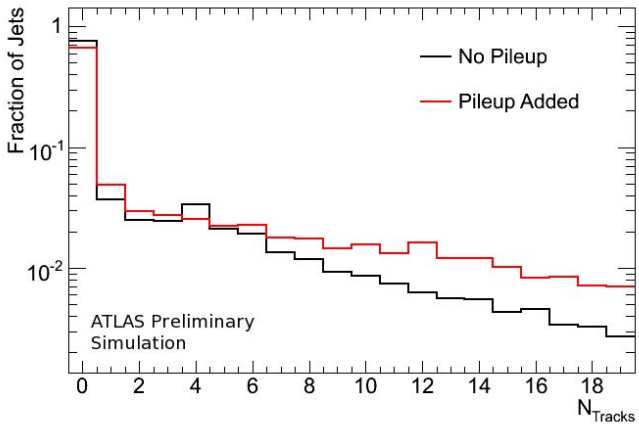

Figure 16: Number of reconstructed tracks ($p_T \geq 1$ GeV) associated with each L2 jet using the SiTrack algorithm in a ($\Delta\eta \times \Delta\phi$) region of ($0.2 \times 0.2$) around the jet axis.

6 Trigger Implementation

In this section we describe the implementation of the new L2 algorithms in the ATLAS High Level Trigger (HLT) framework. Triggers we describe are seeded by L1 triggers present in the current ATLAS trigger menu.

6.1 The Muon RoI Cluster Trigger

The schematic diagram of the sequence of algorithms used for the muon RoI cluster trigger is shown in Figure 17(a). The L1 muon trigger chain (L1_2MU4 is one of the proposed triggers) is used to seed the L2 trigger chain. The Muon RoI Cluster Fex[12)] algorithm first finds the $\Delta R = 0.4$ cone that contains the maximum number of RoIs . Then it looks for jets with $E_T > 35$ GeV, $|\eta| < 2.5$ and $\log_{10}(E_{HAD}/E_{EM}) < 0.5$ in a $\Delta R = 0.7$ cone around the cluster center and next computes the number of tracks with $p_T > 2$ GeV in a ($\Delta\eta \times \Delta\phi$) region of ($0.2 \times 0.2$) around the muon RoI cluster center. The Hypothesis algorithm requires that the cluster contain at least three muon RoIs and no jets or tracks in the regions defined above. No additional requirements are imposed at the Event Filter.

We have considered several possible L1 triggers to seed our L2 muon cluster trigger; they are summarized in Table 3, which gives the efficiencies. The absolute efficiency is the percentage of all generated events (no additional cuts or backgrounds added) that are accepted by the L2 trigger. This efficiency depends on the fraction of events decaying in the muon system and therefore on the proper lifetime of the π_v^0 (see Figure 1). We note that the L2 efficiency relative to L1 with these triggers is in the range 60%-80%. The main difference is in the absolute efficiency. In the following discussion we present results from the L1_3MU6 trigger because it is foreseen not to be prescaled up to a luminosity of about 10^{34} cm^{-2}s^{-1}. For lower luminosities we plan to use the most efficient trigger (L1_2MU4) until bandwidth constraints require that it be prescaled.

[12)] The Fex algorithms compute the features of the object associated with the L1 RoI. These features are subsequently compared against selection conditions in the Hypothesis (Hypo) algorithms.

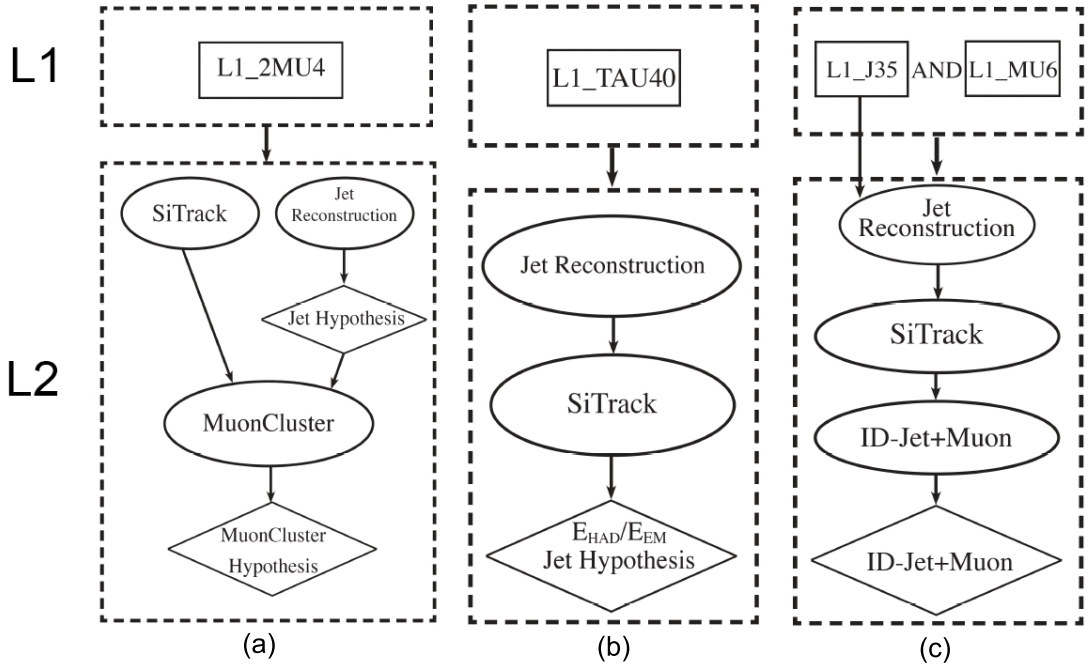

Figure 17: Hidden Valley triggers: schematic diagram of the sequence of algorithms used. The ovals and diamonds represent Feature Extraction algorithms and Hypothesis algorithms, respectively.

6.2 The Calorimeter Energy Ratio Trigger (E_{HAD}/E_{EM})

The logical diagram for the jet energy ratio trigger is shown in Figure 17(b). The trigger starts from the L1_TAU40 item. The L1_J35 jet associated to the L1_TAU40 is used to seed both the jet reconstruction and the SiTrack algorithms. The decision to accept the event is made in the Hypothesis algorithm, which is a modified version of the standard jet Hypothesis algorithm. Acceptance requires to have a jet with $E_T > 35$ GeV, $|\eta| < 2.5$, $\log_{10}(E_{HAD}/E_{EM}) \geq 1$ and no ID tracks with $p_T \geq 1$ GeV in a $(\Delta\eta \times \Delta\phi)$ region of (0.2×0.2) around the jet direction. At the EF, we apply a standard jet EF algorithm to select a jet with $E_T \geq 35$ GeV.

6.3 The ID Trackless Jet with a Muon

The schematic diagram of the sequence of algorithms used for the ID-jet+muon trigger is shown in Figure 17(c). The ID-jet+muon trigger starts from a logical AND between the L1_J35 and L1_MU6 items. The L1_J35 item seeds the standard L2 jet reconstruction algorithm and the SiTrack algorithm. The jet and muon trigger elements seed the Fex ID-jet+muon trigger algorithm. This algorithm looks for

Trigger	L2 Absolute Eff.	L2 Eff. w.r.t. L1
Muon Cluster[L1_3MU6]	9.5%	72.0%
Muon Cluster[L1_2MU4_MU6]	17.1%	79.9%
Muon Cluster[L1_2MU4]	18.7%	62.0%
Muon Cluster[L1_3MU4]	18.7%	78.6%

Table 3: L2 muon cluster trigger efficiency for several L1 items.

the angular matching between a muon RoI and L2 jet in a $\Delta R = 0.4$ region. The jet is required to have $E_T > 35$ GeV, $|\eta| < 2.5$ and no tracks with $p_T \geq 1$ GeV in the $(\Delta\eta \times \Delta\phi)$ region of (0.2×0.2) around the jet direction. If the requests are satisfied the event is accepted.

7 Trigger Timing Issues

In this section we discuss the trigger timing associated with the triggers we have defined and discussed in the previous sections[13]. All of the distributions in this section (except Figure 19) in this section are generator level PYTHIA simulation. The integral distribution of β_{π_v} shown in Figure 3, Section 3, shows that most of the π_v^0 have $\beta > 0.7$. The important issue is to ensure that our triggers, particularly the muon triggers, be associated with the correct beam crossing. The critical parameter to examine is the time shift of our trigger with respect to the trigger from a $\beta \simeq 1$ particle originating at the IP in the same interaction that produced the π_v^0. We note that the hadrons that provide the trigger have $\beta \simeq 1$. Thus in evaluating the time of arrival difference, Δt, between our triggers and a $\beta \simeq 1$ particle from the IP we need only consider the path length of the π_v^0 from the IP to its decay to $b\bar{b}$-pairs.

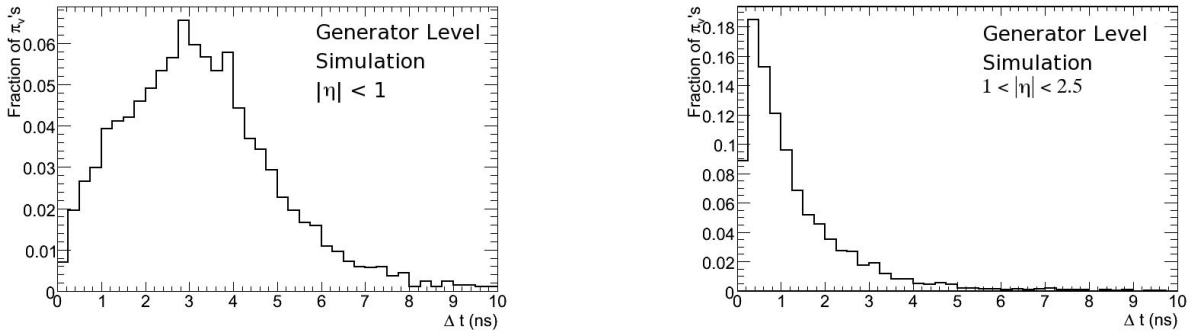

Figure 18: Distribution of Δt shifts for π_v^0's that decay in the Muon Spectrometer.

7.1 The Muon RoI Cluster Trigger

The distribution of Δt shifts for $|\eta| < 1$ (barrel Muon Spectrometer) and for $1 < |\eta| < 2.5$ (endcap Muon Spectrometer) are shown in Figure 18. We note that for $|\eta| < 1$ approximately 80% have less than 6 ns time shift with respect to a $\beta \simeq 1$ particle, and for $1 < |\eta| < 2.5$ nearly 100% of the triggers arrive with less than 4 ns shift. Events that decay in the region $|\eta| > 1$ have high longitudinal momentum and a correspondingly small Δt. We can compare our time shifts to the acceptance window of the muon triggers, which is currently set to fall between beam crossings, that is 12.5 ns following the interaction and 12.5 ns before the next crossing.

Figure 19 shows the efficiency of the muon trigger as measured in the H8 test beam [14]. The window of 100% efficiency is approximately 6 ns. Absent errors in timing calibrations, time shifts beyond this will result in some of the triggers being associated with the next beam crossing in a predictable Gaussian manner. We have used the 6 ns shift in order to evaluate mass parameter ranges over which our triggers are sensitive.

[13] Other mediator decays,like the π_v^0 from Z', are highly boosted over the entire π_v^0 mass range and therefore trigger timing issues are negligible.

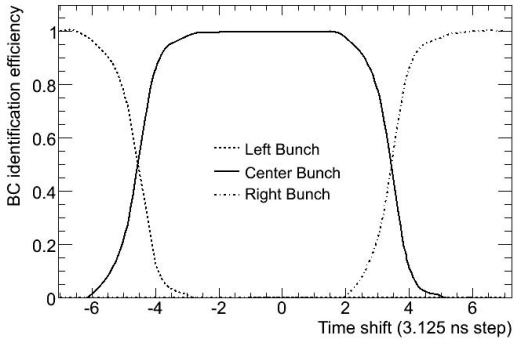

Figure 19: Efficiency of correctly associating the low p_T muon trigger to the correct bunch counter vs the signal delay; one unit of time shift corresponds to 3.125 ns (From [14]).

Figure 20 shows the fraction of π_v^0's with a Δt shift < 6 ns as a function of the π_v^0 mass for Higgs masses between $m_{h^0} = 120$ and 160 GeV. For π_v^0 masses less than about $0.4 m_{h^0}$ the fraction with $\Delta t < 6$ ns is about 70%.

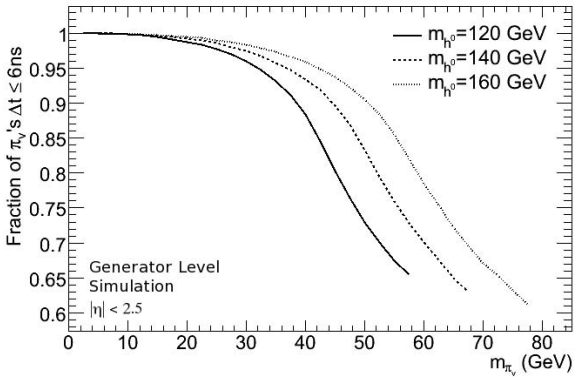

Figure 20: Fraction of π_v^0's with a Δt shift < 6 ns as a function of the π_v^0 mass.

7.2 The Calorimeter Energy Ratio Trigger (E_{HAD}/E_{EM})

The current simulation of the calorimeter trigger correctly handles the time delay which, as shown below, is small. The Δt distributions for events that satisfy our calorimeter energy trigger are shown in Figure 21[14]. Most of the events have less than 3 ns delay. As an example of the kinematic reach of our trigger we show in Figure 22 the fraction of π_v^0 triggers that fall within a 3 ns window of a $\beta \simeq 1$ trigger.

8 Trigger Efficiency and Rates

Trigger efficiencies and rates for both signal and background are presented and discussed in this section. Signal efficiencies are reported for each of the samples defined in Table 1. Signal efficiencies have been determined using both the trigger aware analysis on reconstructed events and running the trigger simulation with the implemented triggers (described in Section 6) on simulated raw data.

[14] The two peaks at approximately 0.5 ns and 2 ns correspond to decays in the endcap and barrel regions, respectively.

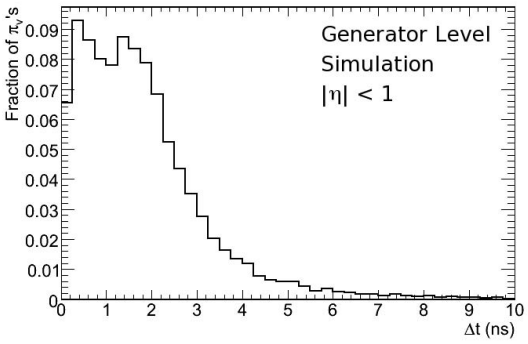

Figure 21: Δt distribution for π_v^0's that decay in the HCal for $m_{h^0} = 140$ GeV and $m_{\pi_v^0} = 40$ GeV.

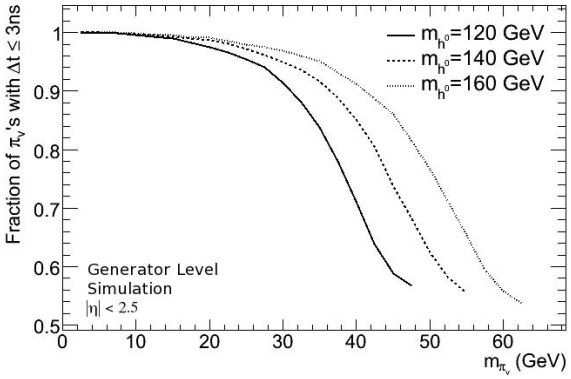

Figure 22: Fraction of π_v^0's that decay in the HCal with a Δt shift < 3 ns as a function of the π_v^0 mass.

8.1 Efficiencies of the Trigger Algorithms

The following tables give the efficiencies obtained running the implemented trigger algorithms on the simulated raw data. Table 4 gives the percentage of generated events passing the L1 and L2 triggers.

Trigger	L1 Absolute Eff.	L2 Absolute Eff.	L2 Eff. w.r.t. L1
Muon Cluster (L1_3MU6)	13.2%	9.5%	72.0%
E_{HAD}/E_{EM} (L1_TAU40)	24.3%	15.1%	62.1%
ID-jet+muon (L1_J35_MU6)	16.5%	3.7%	22.4%

Table 4: L1 and L2 trigger efficiencies: 10 TeV signal sample (15K events). The absolute efficiency is the percentage of all generated events and therefore depends on the specific case we have generated.

The trigger correlation matrices for the L2 triggers, Table 5 and Table 6, give the unique efficiency (diagonal elements), the overlap with the other triggers and the total efficiency for events without and with pileup, respectively. The unique efficiency is the percentage of events that only pass a given trigger and no other. The total efficiency is the sum of the upper triangular matrix elements and does not double count events that satisfy more than one trigger.

L2 Trigger	Muon Cluster	E_{HAD}/E_{EM}	ID-jet+muon	Sum
Muon Cluster	8.5%	0.85%	0.15%	9.5%
E_{HAD}/E_{EM}		12.0%	2.3%	15.1%
ID-jet+muon			1.3%	3.7%

Total Efficiency value: 25.1%

Table 5: L2 trigger unique efficiencies and overlaps: 10 TeV signal sample (15K events).

L2 Trigger	Muon Cluster	E_{HAD}/E_{EM}	ID-jet+muon	Sum
Muon Cluster	8.1%	0.8%	0.2%	9.1%
E_{HAD}/E_{EM}		11.5%	1.9%	14.2%
ID-jet+muon			2.3%	4.4%

Total Efficiency value: 24.8%

Table 6: L2 trigger unique efficiencies and overlaps: 10 TeV signal plus pileup sample (45K events).

8.2 Dependence of Trigger Efficiencies on π_v^0 Decay Length

The relative efficiency of the new signature driven L2 triggers as a function of the π_v^0's decay length is given in this section. We define the relative efficiency as the fraction of π_v^0's decaying at a distance L_R that pass our L2 trigger. For triggering on π_v^0's that decay in the barrel region between the end of the Hadronic Calorimeter (4250 mm) and the first muon trigger plane (7000 mm), the Muon RoI Cluster algorithm is approximately 60 to 70 percent efficient (Figure 23 Left). In the forward region, the trigger is approximately 25% to 30% efficient in the region between the end of the Endcap Calorimeter ($\sim$ 6500 mm) to $\sim$ 12000 mm, after which the efficiency drops because the jets originating from the 5tr5 decay do not sufficiently separate before hitting the muon trigger plane (14000 mm). Pileup has little or no effect on the Muon RoI Cluster trigger.

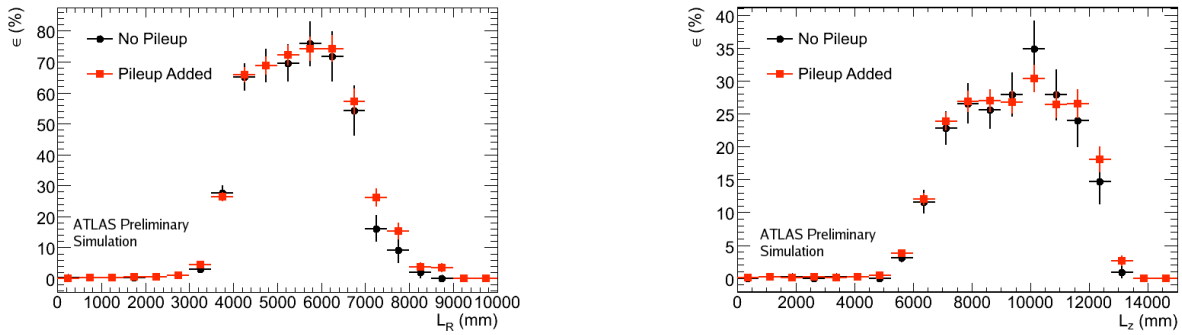

Figure 23: Efficiency for the muon RoI cluster trigger as a function of the π_v^0 decay position for decays in the barrel (Left) and endcap (Right).

Figure 24 gives the efficiency of the $\log_{10}(E_{HAD}/E_{EM})$ trigger. In the barrel region (Left plot), it can be seen that the trigger without pileup is about 75% efficient for π_v^0's that decay in the Hadronic Calorimeter (between 2250 mm and 3500 mm) and becomes less efficient for π_v^0 decays near the end of the calorimeter where there is not a sufficient amount of calorimeter left to contain/measure the jet energy.

As expected, the addition of pileup reduces the trigger efficiency due to additional energy deposited in the Electromagnetic Calorimeter (Left plot). The no-pileup events were simulated with a power supply on one side of the endcap calorimeter turned off, which accounts for the low efficiency of these events. Figure 25 gives the efficiency of the ID Trackless Jet with a Muon trigger. The pileup events contain a greater percentage of muon RoIs which accounts for the higher efficiency of the pileup events. This effect can also be seen in Tables 5 and 6.

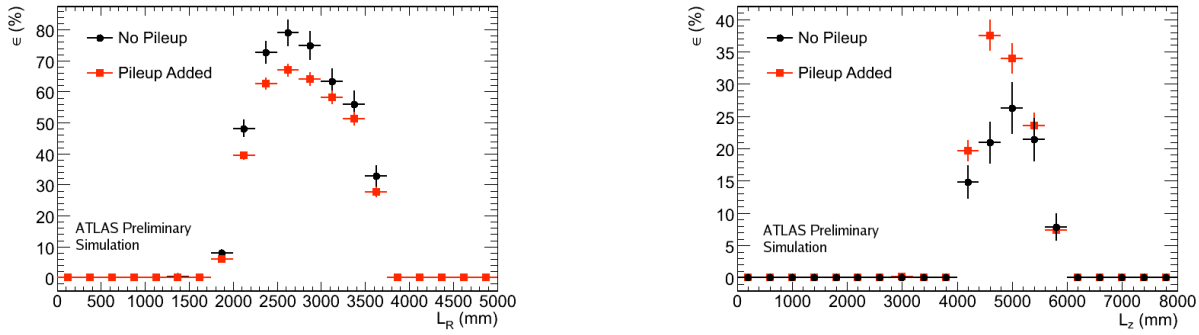

Figure 24: Efficiency for the $\log_{10}(E_{HAD}/E_{EM})$ trigger as a function of the π_v^0 decay position for decays in the barrel (Left) and endcap (Right).

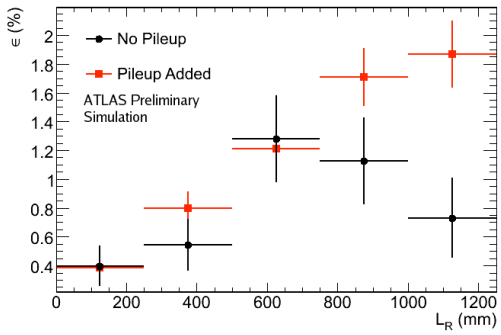

Figure 25: Efficiency for the Trackless Jet + muon trigger as a function of the π_v^0 decay position for decays in the barrel region.

From the efficiency for triggering on a π_v^0 as a function of its decay position, we predict the fraction of Higgs decays that would be accepted by our triggers as a function of the π_v^0 proper lifetime $c\tau$, assuming a 100% branching fraction for $h^0 \to \pi_v^0\pi_v^0$. In order to make this prediction, we generate a set of 300K $h^0 \to \pi_v^0\pi_v^0$ events for a range of lifetimes (from 0 - 20000mm in steps of 200mm) and weight the fraction of π_v^0's that decay in each of our defined detector regions by the probability to detect the π_v^0 decay in that region, Figures 23-25. The error band is derived from the errors shown in these figures. Figure 26 shows the expected fraction of events vs the π_v^0 lifetime for each of our three triggers, and the total fraction accepted. The right scale gives the number of expected events for an integrated luminosity of 100 pb^{-1}.

8.3 Background Studies

The acceptance of our new triggers for QCD di-jets and minimum bias events are discussed in this section. For these studies we applied the signature-driven triggers defined above to simulated raw data

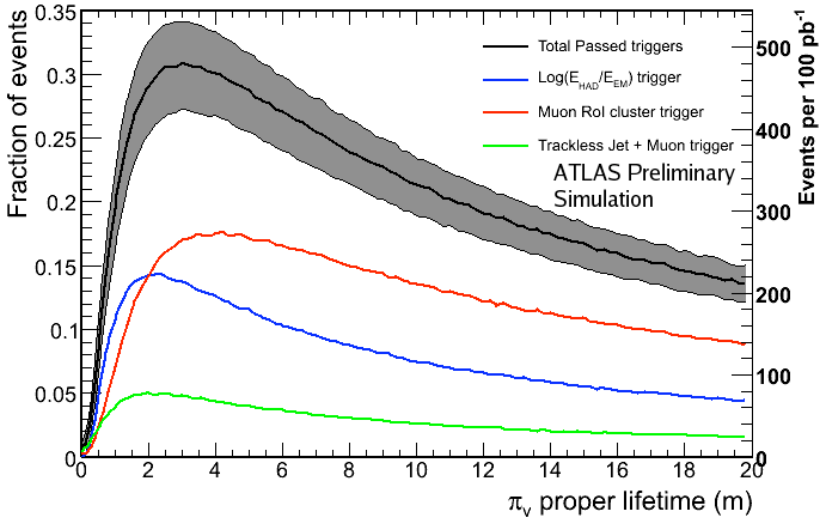

Figure 26: $h^0 \to \pi_v^0 \pi_v^0$ events accepted by our long-lived particle triggers vs the π_v^0 lifetime for $m_{h^0} = 140$ GeV and $m_{\pi_v^0} = 40$ GeV. Left axis: fraction of events accepted. Right axis: number of events for an integrated luminosity of 100 pb^{-1} assuming Br($h^0 \to \pi_v^0 \pi_v^0$)=100%.

generated with the ATLAS-GEANT4 simulation chain. Two 10 TeV QCD di-jet samples were studied: 300K events where the energy of the leading jet is in the range 35 - 70 GeV ($\sigma \sim 56\mu$b) and a second 230K sample where the leading jet is in the range 70 - 140 GeV ($\sigma \sim 3.2\mu$b). The 10 TeV minimum bias sample contains $\sim$ 3M events ($\sigma \sim 51.6$ mb). While no events in this minimum bias sample passed our L2 triggers, the sample corresponds to less than a second of operation at a luminosity of 10^{32} cm^{-2}s^{-1}

The results obtained using the trigger simulation on simulated raw data for the 10 TeV di-jet sample are summarized in Table 7. From these studies we conclude that the contribution to the trigger rate falls with increasing jet E_T due to the rapidly falling cross section of the QCD dijet samples and are within acceptable values. We note that to convincingly understand these backgrounds we need real collision data. The effects of tails of distributions, cracks in the detector and material distribution are a challenge to reliably simulate.

	35 - 70 GeV		70 - 140 GeV	
Trigger	Events	Rate (Hz)	Events	Rate (Hz)
Muon Cluster	21	0.4	22	0.03
ID-jet+muon	21	0.4	71	0.10
E_{HAD}/E_{EM}	5	0.1	10	0.01

Table 7: Trigger rates for 10 TeV QCD di-jet samples at a luminosity of 10^{32}cm^{-2}s^{-1}.

9 Conclusions

A number of extensions of the Standard Model predict new particles that are neutral and with a lifetime comparable with ATLAS detector dimensions. In this note we have shown that it is necessary to define

a set of signature-driven triggers in order to select this type of events with a reasonable efficiency. Algorithms for these triggers have been implemented in the ATLAS High Level Trigger framework. An evaluation of these new triggers using the full ATLAS simulation chain has been presented both for the signal and for some main expected backgrounds. Good efficiency for the signal has been obtained. While this study indicates that the background rates should be acceptable at low luminosities, to fully understand background problems we will need real data to be able to properly assess pile-up, QCD di-jets and cosmic backgrounds. This we plan to do during early operation and adjust our triggers as necessary.

References

[1] G. Aad et al., The ATLAS Collaboration, JINST 3 S08003.

[2] L. J. Hall and M. Suzuki, Nucl. Phys. B **231**, 419 (1984).

[3] S. Dimopoulos, M. Dine, S. Raby and S. D. Thomas, Phys. Rev. Lett. **76**, 3494 (1996) [arXiv:hep-ph/9601367]. C. H. Chen and J. F. Gunion, Phys. Rev. D **58**, 075005 (1998) [arXiv:hep-ph/9802252].

[4] U. Ellwanger and C. Hugonie, Eur. Phys. J. C **13**, 681 (2000) [arXiv:hep-ph/9812427]. Phys. Rev. D **62**, 095008 (2000) [arXiv:hep-ph/0005116]; S. Hesselbach, F. Franke and H. Fraas, Phys. Lett. B **492**, 140 (2000) [arXiv:hep-ph/0007310].

[5] K. T. Matchev and S. D. Thomas, Phys. Rev. D **62**, 077702 (2000) [arXiv:hep-ph/9908482].

[6] N. Arkani-Hamed and S. Dimopoulos, JHEP **0506**, 073 (2005) [arXiv:hep-th/0405159]; A. Arvanitaki, S. Dimopoulos, A. Pierce, S. Rajendran and J. Wacker, arXiv:hep-ph/0506242.

[7] M. J. Strassler and K. M. Zurek, Phys. Lett. B 651 (2007) 374-379.

[8] M. J. Strassler and K. M. Zurek, Phys. Lett. B 661 (2008) 263-267.

[9] M. J. Strassler, arXiv:hep-ph/0607160.

[10] S. Chang, P. J. Fox and N. Weiner, JHEP 0608 (2006) 068.

[11] L. M. Carpenter, D. E. Kaplan and E. J. Rhee, arXiv:hep-ph/0607204.

[12] T. Sjostrand, S. Mrenna, and P. Skands arXiv:hep-ph/0603175.

[13] G. Aad et al. The ATLAS Collaboration, arXiv:0901.0512.

[14] C. Adorisio et al., Nucl. Inst. and Meth. A593, 2008, p.400.